



Article

Hydrothermal Synthesis of FeOOH and Fe₂O₃ Modified Self-Organizing Immobilized TiO₂ Nanotubes for Photocatalytic Degradation of 1H-Benzotriazole

Tihana Čižmar¹, Vedran Kojić¹, Marko Rukavina², Lidija Brkljačić¹, Krešimir Salamon¹, Ivana Grčić³ , Lucija Radetić³ and Andreja Gajović^{1,*} 

¹ Ruđer Bošković Institute, Bijenička 54, HR-10000 Zagreb, Croatia; tihana.cizmar@irb.hr (T.Č.); Vedran.Kojic@irb.hr (V.K.); lidija.brkljacic@irb.hr (L.B.); Kresimir.Salamon@irb.hr (K.S.)

² Termoterra d.o.o., Donja Čemernica 151, HR-44415 Topusko, Croatia; marko@termoterra.hr

³ Faculty of Geotechnical Engineering, University of Zagreb, Hallerova Aleja 7, HR-42000 Varaždin, Croatia; igrcic@gfv.hr (I.G.); lradetic@gfv.hr (L.R.)

* Correspondence: gajovic@irb.hr

Received: 5 October 2020; Accepted: 24 November 2020; Published: 24 November 2020



Abstract: In this study, titanium dioxide nanotubes were prepared by electrochemical anodization technique and modified with an aqueous solution of FeCl₃ using hydrothermal synthesis method to control the amount and distribution of iron compounds on the anatase TiO₂ nanotubes. The objective was to synthesize immobilized FeOOH@TiO₂ or Fe₂O₃@TiO₂ photocatalysts designed for the flow-through reactor systems; to investigate thermal treatment effect on the photocatalytic efficiency; to determine appropriate Fe-compounds concentration for the maximum photocatalytic activity improvement, and to explain the mechanism responsible for the enhancement. The photocatalysts were tested for the degradation of 1H-benzotriazole in water under UV/solar light irradiation. Up to two times increase in the photocatalytic activity was obtained when TiO₂ nanotubes were modified with 0.8 mM Fe. At higher Fe concentrations (8 mM and 80 mM), the photocatalytic activity of the given photocatalysts decreased. To confirm the formation of FeOOH or Fe₂O₃ species, and to clarify the mechanism of photoactivity, X-ray diffraction (XRD), Raman spectroscopy (RS), Scanning Electron Microscopy (SEM) and Energy Dispersive X-ray spectroscopy (EDS) and UV-Vis spectroscopy were used.

Keywords: TiO₂ nanotubes; FeOOH and Fe₂O₃ modified immobilized TiO₂ photocatalysts; hydrothermal synthesis; photocatalytic activity; 1H-benzotriazole

1. Introduction

In an ever growing field of photo catalysis, titanium dioxide (TiO₂) is one of the most prominent materials used to date. The foundation was set by Fujishima [1] in 1972 for their research on water splitting based only on irradiating the TiO₂ electrode with UV light. Large interest in TiO₂ is derived from its high stability, low industrial cost and abundance, high biocompatibility and simple synthesis procedures [2–4]. With the combination of rising awareness towards human environmental impact, research was initiated towards efficient and cheap materials to be used in air [5] and water [6] purification treatments.

TiO₂ occurs in three different polymorphs: rutile, anatase and brookite [7]. While rutile is the most thermodynamically stable polymorph form, one that shows the best impact in photocatalysis is the anatase phase [8]. If TiO₂ is irradiated with light containing energy equivalent to 3.2 eV or

higher (for anatase polymorph), electrons inside the valence band (VB) are able to transit into the conduction band (CB). Valence band is left with vacancies called holes which can react with electron donor species (hydroxyl ions), thus creating radicals. Similar mechanism happens in the conduction band with the excess amount of electrons reacting with electron accepting species (oxygen molecules) in which radicals are also formed. The mechanism of pollutant degradation is based upon generating and controlling radical species and using them to react with pollutants.

Another benefit TiO_2 offers as a material is the ability to synthesize in 1D nanostructures. Several recent reviews assess this topic [9,10]. Nanostructured TiO_2 offers high specific area while retaining material stability as well as enhancing optoelectronic properties due to quantum size effects that arise as a consequence of nanoscale dimensions. The discovery of Grimes and colleagues [11] for the electrochemical anodization of titanium foil to obtain TiO_2 nanotubes offered a low cost and scalable method to synthesize and control the morphology of the material (nanotube length, film thickness, tube wall thickness as well as the specific surface) paving the way for the future modifications.

Naturally, TiO_2 has its drawbacks: the bandgap of the anatase phase corresponds to the wavelength of 384 nm which means only the UV fraction of the solar spectrum can be harvested, accounting for approx. 5% of the available spectrum [12]. Therefore, it is understandable that research towards modification of TiO_2 is being conducted in order to combine materials with favorable properties and to mitigate the limitations of TiO_2 .

There are several methods by which TiO_2 can be modified with various metallic and nonmetallic elements such as nitrogen [13], sulfur [14], gold [15], platinum [16], silver [17], iron [18], copper [19]; surface modifications with acids such as sulfuric acid [20] or fluorides [21]; modification with various polymers like polyaniline [22] or polythiophene [23]. Another approach to the modification of TiO_2 is by using different modification techniques such as chemical vapor deposition [24], atomic layer deposition [25], sol-gel method [26] and hydrothermal method [27]. Hydrothermal method shows promising results for the decoration as, for example, in the case of cadmium sulfide [28], iron oxide [29,30], and silicon [31]. With increased temperature and pressure, the dissolution of precursors and the reaction rate are accelerated.

Transition metal oxide materials (Bi_2O_3 , WO_3 , ZnO , Fe_2O_3) have promising characteristics for photocatalytic applications. They are stable, non-toxic, inexpensive materials and can tune the band gap towards visible light irradiation. As a consequence of inferior conductivity, low diffusion lengths of holes and high charge carrier recombination rates, the electrons at the conduction band cannot be trapped by O_2 to yield superoxide radicals. Heterojunctions between various metal oxide semiconductors are investigated in order to efficiently separate charge carriers [32]. Spanu et al. [33] demonstrated that a layered structure on TiO_2 nanotubes, which combines both metallic (Pt) and semiconductor (WO_3) modifications, enhanced the evolution of hydrogen. Wei et al. [34] showed how approach regarding matching electronic band structures on heterojunctions between two semiconductors can suppress the recombination of photogenerated electrons and holes, which ultimately leads to the improved photocatalytic activity. Spanu et al. [35] synthesized $\alpha\text{-Fe}_2\text{O}_3$ photoanodes that showed improved photocatalytic yield with pre-polarization of working photoanodes. In their systematic review on applicability of magnetic iron oxides, Singh et al. [36] explained the influence of electronic structure, morphology and various synthesis techniques on iron oxide photodegradation of organic pollutants in water.

Iron oxides (Fe_2O_3 , FeOOH) are suitable modification candidates that ensure low-cost and practical approach to TiO_2 photocatalysis yield improvement. Furthermore, their band gaps are in visible light range (1.7–2.3 eV for FeOOH [37,38] and 1.9–2.5 eV for Fe_2O_3 [39]) and thus, by combining the superior semiconducting properties of TiO_2 and broader photon absorption energy span of iron oxides, photocatalytic properties of TiO_2 nanotubes can be improved due to synergistic effect between iron species and TiO_2 [40–42].

In the system similar to ours, where TiO_2 NTs were pre-loaded with $\text{Fe}(\text{OH})_3$ using sequential chemical bath deposition, Kuang et al. [43] demonstrated how improved separation efficiency of

photogenerated e^-/h^+ enhanced photoelectrochemical performances. Furthermore, Cong et al. [44] synthesized hetero-nanostructure of $\alpha\text{-Fe}_2\text{O}_3/\text{TiO}_2$ nanotubes by electrochemical deposition method for photoelectro-Fenton degradation of phenol. They reported an improved nanophotocatalysts response to visible light, thus highlighting the role of Fe_2O_3 NPs in photoelectro-Fenton process.

In widely studied field of photocatalytic materials, especially TiO_2 decorated with semiconductor oxides such as iron oxides, emphasis should be on environmentally friendly, fast and inexpensive synthesis which can yield an effective photocatalyst. Furthermore, the separation of transition metal catalyst from the catalytic solution is a major problem, hence immobilization of the photocatalyst is a logical approach since there is no need for the additional purification after photocatalytic reaction. That being the case, the objectives of this study included: inexpensive and fast synthesis of immobilized FeOOH@TiO_2 or $\text{Fe}_2\text{O}_3\text{@TiO}_2$ photocatalysts designed for the flow-through reactor systems photocatalysis; investigation of thermal treatment effect (transformation of FeOOH to Fe_2O_3) on the photocatalytic efficiency; and determination of appropriate Fe-compounds concentration for the photocatalytic activity improvement of pure immobilized nanostructured TiO_2 . In this research we studied the influence of both FeOOH and Fe_2O_3 modifications on photocatalytic response of TiO_2 nanotubes for degradation of 1H-benzotriazole. TiO_2 nanotubes were synthesized via electrochemical anodization technique and modified with FeOOH and Fe_2O_3 using hydrothermal synthesis method in a neutral aqueous medium with the aim to control concentration and distribution of iron species on the anatase TiO_2 nanotubes. In order to compare oxidation efficiency, 1H-benzotriazole, a model heterocyclic compound, used as a corrosion inhibitor and as a drug precursor in the pharmaceutical industry (being a relevant pollutant in aquatic environments), was used [45].

2. Results and Discussion

2.1. Structural and Optical Properties of the Photocatalysts

To clarify the mechanism responsible for the photocatalytic activity improvement in studied catalysts, different spectroscopic and analytical techniques were used to determine the morphology and crystal structures present in unmodified and FeOOH or Fe_2O_3 modified TiNT photocatalysts. Structural phase composition of the samples was examined by confocal micro-Raman spectroscopy, the morphology was investigated by scanning electron microscopy (SEM) and crystal structure was examined by the grazing incidence X-ray diffraction (GIXRD), while optical properties were studied using UV-Vis spectroscopy.

2.1.1. Raman Spectroscopy Results

Figure 1 shows confocal micro-Raman spectra of (a) FeOOH modified TiNT and (b) Fe_2O_3 modified TiNT samples. In all samples, five characteristic bands assigned to anatase TiO_2 crystalline phase ($144, 199, 396, 514,$ and 636 cm^{-1}) are found [46]. Rutile bands were not observed in Raman spectra, although small amount of rutile phase of TiO_2 was detected using grazing incidence X-ray diffraction (GIXRD) analysis (see Section 2.1.3). This discrepancy can be explained by a small amount of rutile and lower intensities of rutile bands in comparison to the anatase bands in Raman spectra. Moreover, for titanium nanotubes modified with FeOOH in various concentrations (0.8 mM, 8 mM and 80 mM, respectively), only spectrum of the sample modified with 80 mM (80 mM_ FeOOH) showed the most prominent characteristic FeOOH band at 250 cm^{-1} [47]. This observation is expected given the fact that in two other samples, the amount and particle size of formed FeOOH is under detection limit of Raman spectroscopy technique. On the other hand, TiNT samples modified with Fe_2O_3 , showed well-established Fe_2O_3 bands visible at 225 and 293 cm^{-1} [47] in 80 mM sample (80 mM_ Fe_2O_3). Additionally, these bands were also observed in 8 mM sample (8 mM_ Fe_2O_3), although having weak intensities. Such results indicate formation of larger Fe_2O_3 crystallites, detectable with Raman spectroscopy, which is in an agreement with SEM results, as it will be shown later.

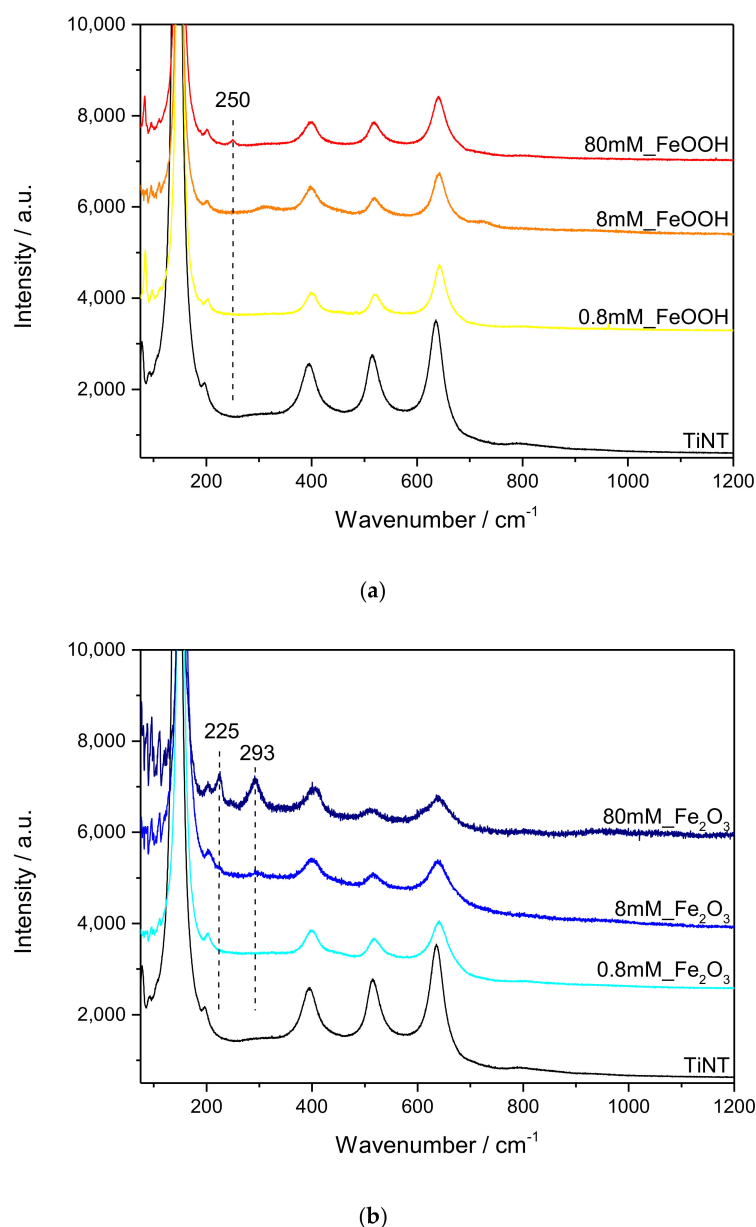


Figure 1. Micro-Raman spectra of (a) FeOOH modified TiNT and (b) Fe₂O₃ modified TiNT samples with specific Raman active bands of Fe modifiers denoted above spectra.

2.1.2. Scanning Electron Microscopy Results

The morphology of the FeOOH@TiNT and Fe₂O₃@TiNT samples was examined with the scanning electron microscope (Figures 2 and 3). TiNT were formed by an electrochemical anodization of Ti foil (see Section 3). The unmodified surface consists of a well-organized and homogeneously arranged nanotubes with an average diameter of 100 nm [48]. FeOOH@TiNT samples, modified with three different concentrations of Fe compounds (0.8 mM, 8 mM and 80 mM), showed significant changes in the morphology, in comparison to as-prepared TiNT. With the increase of FeOOH concentration, amount of nano-structures formed on the TiNT surface also increased. Similarly, after the heat treatment, Fe₂O₃ nano-structures appeared on the surface of TiNTs. The top view images of the 80 mM FeOOH and 80 mM Fe₂O₃ TiNTs reveal that the TiO₂ NTs are completely covered with the iron species (Figures 2c and 3c).

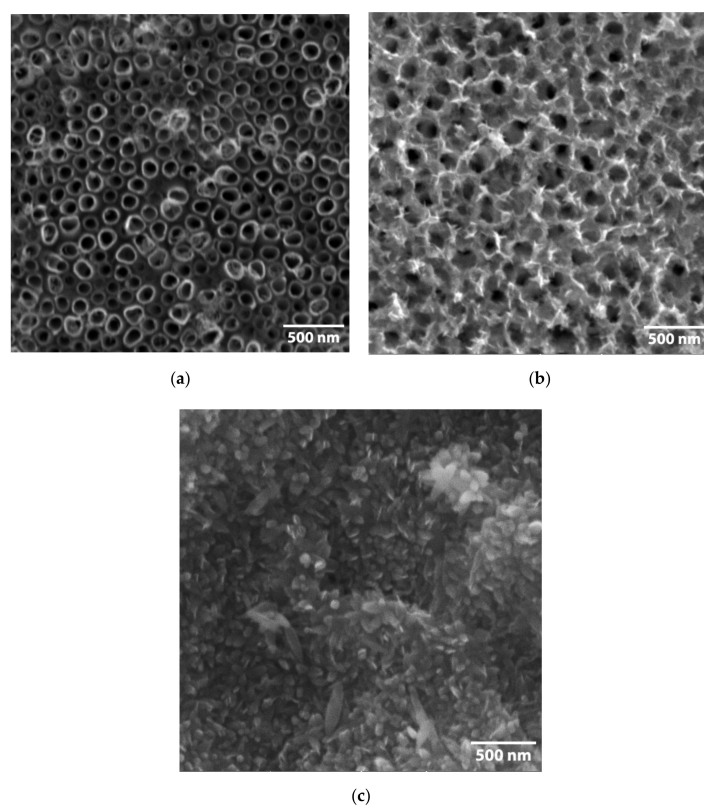


Figure 2. Micrographs of the FeOOH-modified TiNT with three different concentrations of Fe compounds: (a) 0.8 mM, (b) 8 mM and (c) 80 mM.

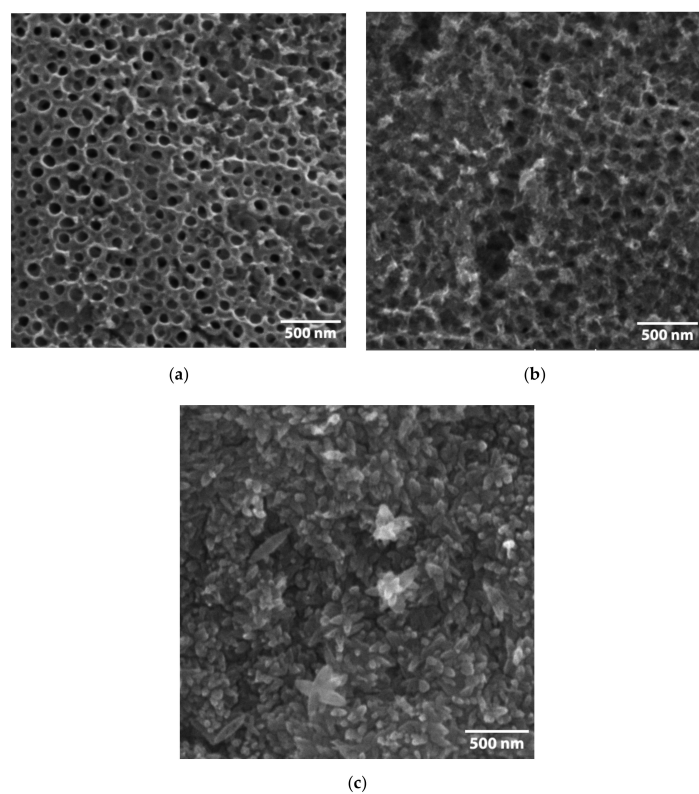


Figure 3. Micrographs of the Fe₂O₃-modified TiNT with three different Fe compounds concentrations: (a) 0.8 mM, (b) 8 mM and (c) 80 mM.

The elemental composition of the FeOOH or Fe₂O₃ modified TiO₂ nanotubes was analyzed using energy dispersive X-ray spectroscopy (EDS) (Table 1). The large area of the samples (using small magnifications of SEM) was used for analysis. It was observed that in both FeOOH@TiNT and Fe₂O₃@TiNT samples the amount (at. %) of Fe increased with the increase of Fe compounds (FeCl₃ aqueous solution) in the reaction. After transformation of FeOOH@TiNT to Fe₂O₃@TiNT by thermal treatment, higher percentages of Fe were observed in Fe₂O₃@TiNT samples than in corresponding FeOOH@TiNT starting samples. This can be explained with iron to oxygen ratio in the two compounds, since in Fe₂O₃ the ratio is Fe:O = 2:3, while in FeOOH it is 1:2.

Table 1. Results of EDS measurements.

Sample	Ti K (at. %)	O K (at. %)	Fe K (at. %)
TiNT	31.23	68.77	0
0.8 mM_FeOOH	29.32	70.53	0.15
8 mM_FeOOH	23.51	73.15	3.34
80 mM_FeOOH	12.37	73.27	14.36
0.8 mM_Fe ₂ O ₃	28.98	70.67	0.35
8 mM_Fe ₂ O ₃	21.44	70.62	7.94
80 mM_Fe ₂ O ₃	10.64	71.31	18.05

2.1.3. Grazing Incidence X-ray Diffraction (GIXRD) Results

GIXRD patterns of all samples are shown in Figure 4 along with reference diffraction profiles for anatase TiO₂ (JCPDS card no. 21-1272), rutile TiO₂ (JCPDS card no. 21-1276), α -Fe₂O₃ (JCPDS card no. 33-0664), β -FeOOH (JCPDS card no. 34-1266) and hexagonal α -Ti substrate (JCPDS card no. 44-1294) which were used for the identification of diffraction peaks and determination of phase composition in samples. The patterns of 0.8 mM_FeOOH and 8 mM_FeOOH samples disclose dominantly anatase TiO₂ with small fractions of rutile TiO₂ phase (~10% for 0.8 mM_FeOOH, ~5% for 8 mM_FeOOH). In the 80 mM_FeOOH sample anatase-TiO₂ (~60%) and tetragonal β -FeOOH (~30%) were observed. Furthermore, the 0.8 mM_Fe₂O₃ and 8 mM_Fe₂O₃ samples disclose anatase TiO₂ as a major phase, but also rutile TiO₂ and α -Fe₂O₃ phases (~5% for each phase). Finally, the phase composition of the 80 mM_Fe₂O₃ sample is similar to the composition of 0.8 mM_Fe₂O₃ and 8 mM_Fe₂O₃ samples, however, the fraction of rutile TiO₂ is reduced and the fraction of α -Fe₂O₃ is increased.

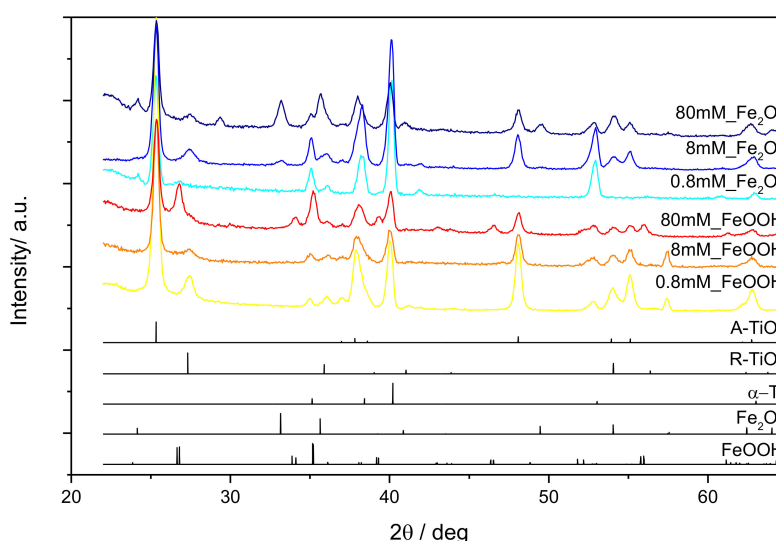


Figure 4. GIXRD diffractograms of FeOOH@TiNT and Fe₂O₃@TiNT samples with different concentration of Fe compounds (0.8 mM, 8 mM and 80 mM).

2.1.4. UV-Vis Spectroscopy Results

The UV-vis reflectance spectra of the FeOOH and Fe₂O₃ modified TiNT are shown in Figure 5a. The TiNT display the absorption edge in UV region at ~385 nm. With addition of 0.8 mM, 8 mM and 80 mM FeOOH and Fe₂O₃, absorption edge shifted towards higher wavelengths. The values of the indirect band gap were obtained by extrapolating the Tauc plot of the Kubelka–Munk function by drawing the line to the x -axis at $[F(R)h\nu]^{1/2} = 0$ (Figure 5b). The band gap for TiNT is estimated to be 3.22 eV. Furthermore, for 0.8 mM_FeOOH, 0.8 mM_Fe₂O₃, 8 mM_FeOOH, 8 mM_Fe₂O₃, 80 mM_FeOOH, 80 mM_Fe₂O₃ samples, band gaps are 3.15 eV, 3.19 eV, 1.91, 1.85, 1.85, 1.79 eV respectively. The narrowing of band gap is due to the coupling of TiO₂ with FeOOH and Fe₂O₃ species on the surface [49,50]. Higher absorption in the visible light region allows the photocatalyst to harness visible light for photocatalytic reactions.

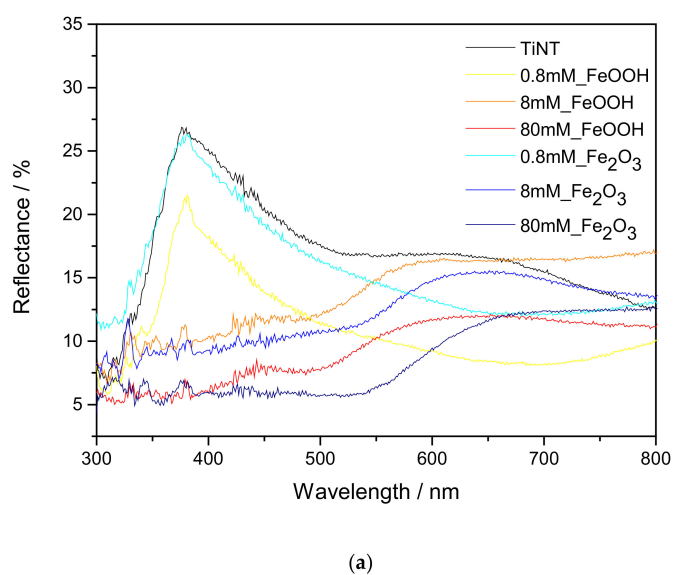


Figure 5. Cont.

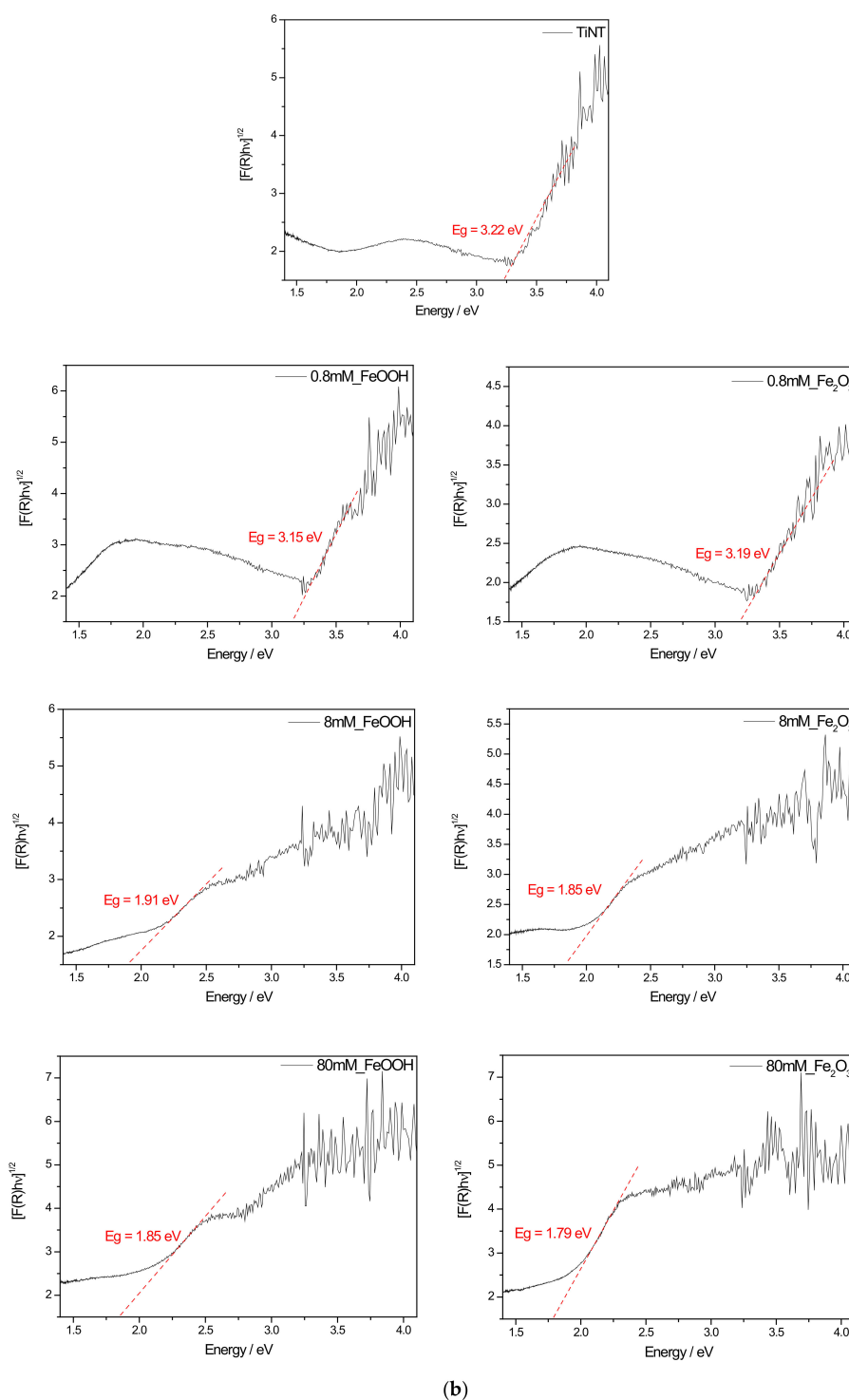


Figure 5. UV-Vis spectroscopy results: (a) Diffuse reflectance spectra of unmodified and FeOOH or Fe₂O₃ modified TiNT and corresponding (b) Kubelka-Munk plots with determined band gap for each sample.

2.2. Photocatalytic Activity

In comparison to TiO₂ P25, which is mostly used in the batch reactor systems, our immobilized FeOOH@TiO₂ and Fe₂O₃@TiO₂ photocatalysts were designed for the flow-through reactor systems. The photocatalytic activity of prepared catalysts was tested under artificial solar irradiation using 1H-benzotriazole (BT) as a model pollutant. All the photocatalytic samples have very small circular

surface area (0.5 cm^2) and the initial BT concentration was adjusted accordingly to match the potential pollutant concentration in the nature ($C_0 \approx 5 \text{ mg dm}^{-3}$).

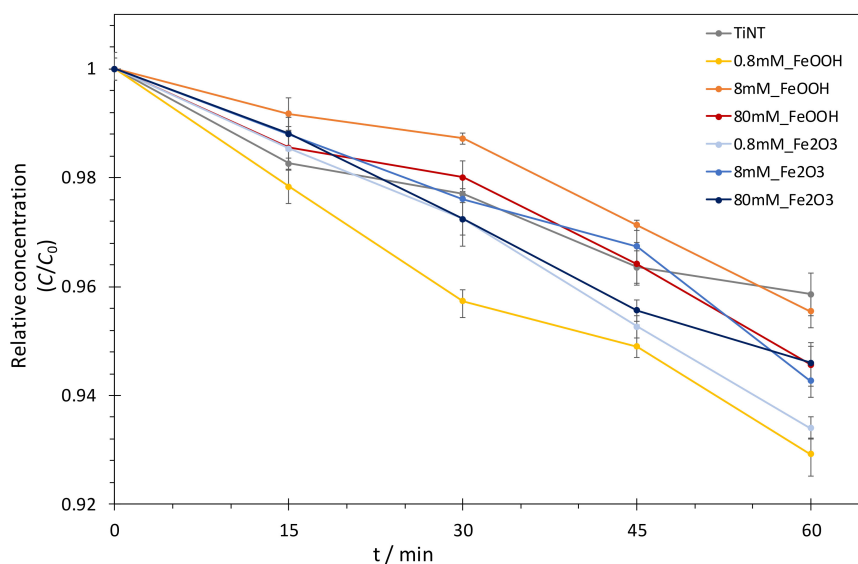
The rate constant (k) was used to compare photocatalytic activity between the reference sample (as-prepared TiO_2 anatase nanotubes (TiNT)) and FeOOH or Fe_2O_3 modified TiNT. Synthesis and FeOOH or Fe_2O_3 @TiNT modification details are explained in the section Materials and methods (see Section 3.1). Modelling of the experimental data (BT concentration as a function of UV/Vis illumination time) was performed according to the pseudo-first order kinetics model (Equation (1)) [51,52]:

$$\ln(C_t/C_0) = -kt \quad (1)$$

where C_0 and C_t represent BT concentrations at the beginning of photodegradation and at time t , respectively, while k is the rate constant. Best fit values for the rate constants (k), obtained for as-prepared TiNT and FeOOH or Fe_2O_3 @TiNT photocatalysts with different Fe loadings, are presented in Table 2 and showed on Figures 6 and 7. The numerical comparison of the photocatalytic activity of TiNT and commercial TiO_2 (P25) was explained in our previous work [17]. The study confirmed similar photocatalytic activity of P25 and TiNT in UV/Vis spectral range, thus, increase in the photocatalytic activity of FeOOH or Fe_2O_3 modified TiNT can be assigned only to the iron modifications.

Table 2. Photocatalysts overview with obtained corresponding rate constants k (pseudo-first order kinetic model).

Name	Sample	$k \text{ (BT)/min}^{-1}$	R^2
TiNT	TiO_2 nanotubes	0.00068	0.9495
0.8 mM_FeOOH	0.8 mM_FeOOH@TiNT	0.00123	0.9858
8 mM_FeOOH	8 mM_FeOOH@TiNT	0.00081	0.9346
80 mM_FeOOH	80 mM_FeOOH@TiNT	0.00066	0.9683
0.8 mM_Fe ₂ O ₃	0.8 mM_Fe ₂ O ₃ @TiNT	0.00111	0.9885
8 mM_Fe ₂ O ₃	8 mM_Fe ₂ O ₃ @TiNT	0.00076	0.9569
80 mM_Fe ₂ O ₃	80 mM_Fe ₂ O ₃ @TiNT	0.00073	0.9933



(a)

Figure 6. Cont.

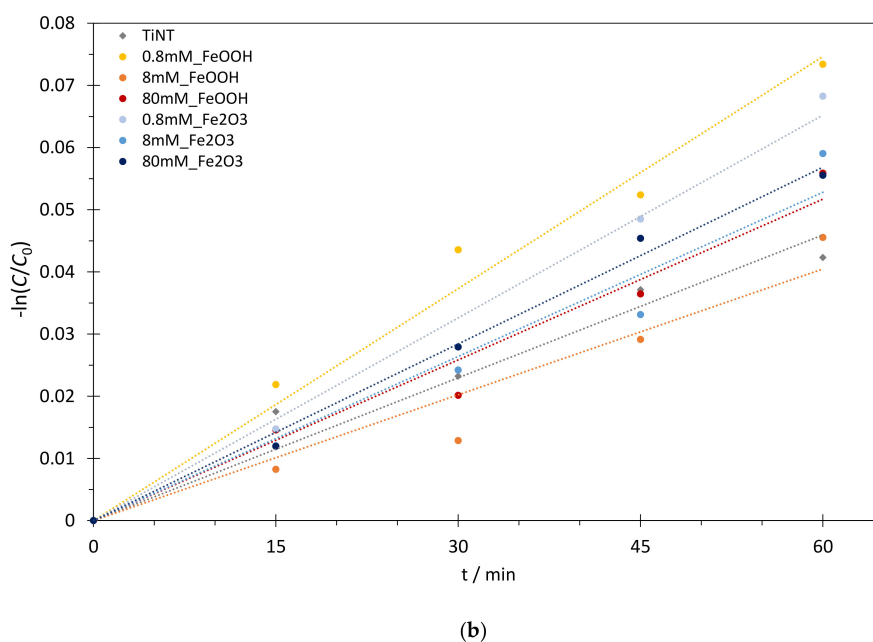


Figure 6. (a) Photocatalytic degradation kinetics of BT and (b) pseudo-first order reaction model: photocatalysis over different FeOOH@TiNT and Fe₂O₃@TiNT photocatalysts under UV/Vis irradiation.

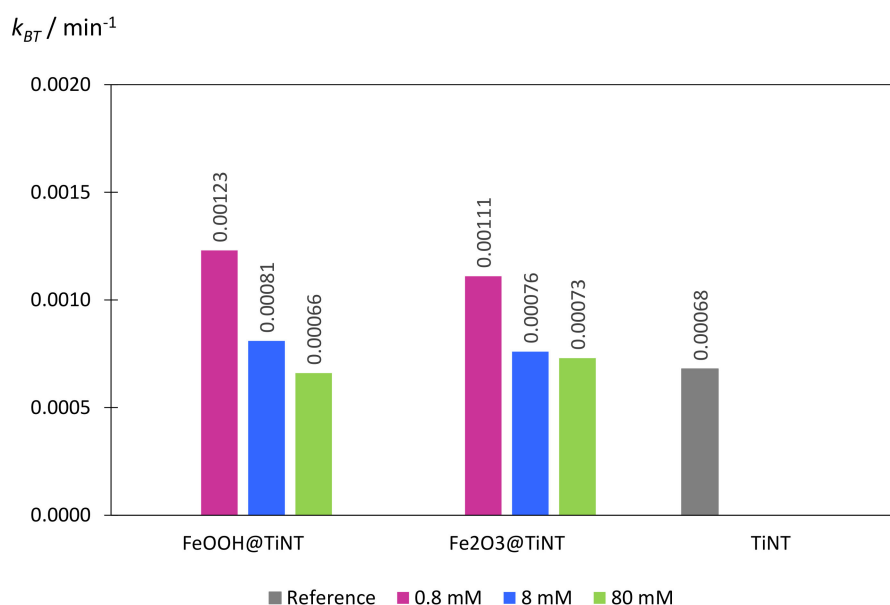


Figure 7. Comparison of the observed first-order rate constants (k_{BT} , min^{-1}) obtained for photocatalytic degradation of 1H-benzotriazole (BT) in SPC reactor over a variety of photocatalysts.

Before photocatalytic measurements, catalyst samples were put in a small photocatalytic cell (SPC) in the dark for 15 min to achieve adsorption equilibrium (Figure 8, gray region). Therefore, decrease of BT concentration in the aqueous solution observed after stirring in the dark is a direct consequence of BT adsorption on the photocatalyst's surface not the BT degradation. The adsorption in dark was additionally tested for 2 h for the best photocatalysts in order to elucidate the effect of the adsorption of BT on the catalyst's surface. It was shown that no significantly relevant additional adsorption happened, indicating that adsorption-desorption equilibrium at the catalyst's surface was already achieved after approximately 15 min in the dark (difference in the adsorption for 15 min and 120 min was below 10%).

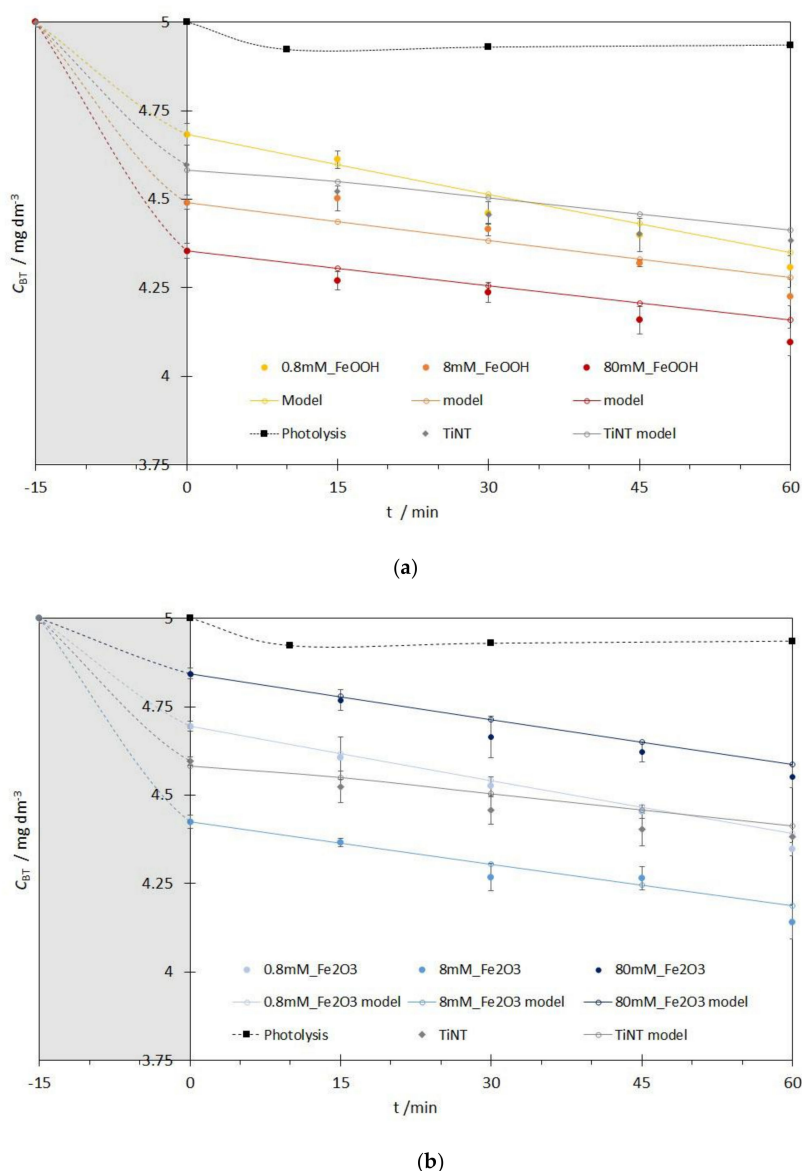


Figure 8. Adsorption in dark (grey regions) and kinetics of the photocatalytic degradation of BT with the pseudo-first order kinetic reaction model for: (a) FeOOH@TiNT photocatalysts with different Fe concentrations, (b) Figure 2. O₃@TiNT photocatalysts with different Fe concentrations.

Depending on the photocatalyst, differences in the adsorption of the BT in the dark were observed. For the FeOOH@TiNT sample with the highest Fe concentration (80 mM_FeOOH), most prominent adsorption was observed (Figure 8a, grey region). With the decrease of Fe concentration (8 mM_FeOOH and 0.8 mM_FeOOH), adsorption decreased as well. That can be explained with the higher number of possible sites where hydrogen bonds (O-H) can be established between photocatalyst and the model pollutant.

The adsorption of BT in the dark on the Fe₂O₃@TiNT photocatalysts' surface does not follow the same trend as the one described above. Sample with the highest Fe concentration (80 mM_Fe₂O₃) showed lowest adsorption (Figure 8b). That can be attributed to the thermal dehydroxylation process occurring during the transformation of the α -Fe₂O₃ [53]. Dehydroxylation could also be responsible for lower formation rate of $\bullet\text{OH}$ radicals during the photocatalytic process.

Photocatalytic degradation process started after BT adsorption-desorption equilibrium was achieved and it was evaluated for 60 min for all the studied photocatalysts. Although Benzotriazoles are prone to photolysis under sunlight irradiation, that reaction is rather slow. It is well known that

irradiation intensity can determine photolysis efficiency [54–56], but in our experiments photolysis contribution to the direct BT degradation is negligible despite the fact that BT is subjected to a direct photolysis under UV/Vis irradiation (black squares in Figure 8a,b). Reaction responsible for BT removal is a direct oxidation with hydroxyl radicals ($\bullet\text{OH}$) [55]. The suggested mechanism of BT degradation by the hydroxyl radicals was based on a previously conducted experiments where we used a simple test with methanol—a well-known scavenger of hydroxyl radicals. During methanol reaction with hydroxyl radicals, dominant reaction is H-atom abstraction from the aliphatic chain, which consequently leads to the formaldehyde formation. Instead of detecting formaldehyde in our system, we monitored the absence of BT degradation in the presence of methanol, thus avoiding development and incorporation of another HPLC method. More importantly, we avoided possible difficulties in the determination of formaldehyde concentrations since we worked with low, but environmentally relevant BT concentrations ($C_{\text{BT}} = 5 \text{ ppm}$). The photocatalytic experiments were performed with equimolar concentrations of BT and methanol and 10 times higher concentration of methanol in comparison to the initial BT concentration. With the introduction of methanol in the system (hydroxyl radical's scavenger), decrease of the BT degradation was expected. Aliquots were taken after 30 and 60 min and analyzed by HPLC. Results showed that BT removal rate decreased when equimolar solution was used. Nevertheless, due to the competing reactions, a low rate ($\sim 1\%$) of BT removal was observed, which was eliminated with the introduction of 10 times higher methanol concentration.

The photocatalytic activity (first-order rate constants) of TiNT increased approximately 2 times when TiNT were modified with 0.8 mM Fe in the form of FeOOH (0.8 mM_FeOOH), and 1.4 times when 0.8 mM_FeOOH sample, which was additionally thermally treated, formed Fe_2O_3 on the surface of TiNT (0.8 mM_Fe $_2\text{O}_3$) (Figure 6 and Table 2). As it was already mentioned, the photocatalytic activity of TiNT is similar to one of commercial TiO_2 (P25) [17]. Therefore, we synthesized series of immobilized TiNT photocatalysts, modified with FeOOH and Fe_2O_3 , with improved photocatalytic activity in comparison the commercial P25 photocatalyst. The increase of the photocatalytic activity for the lowest Fe concentration (0.8 mM) and decrease for higher Fe concentrations (8 mM and 80 mM) in both FeOOH@TiNT and Fe_2O_3 @TiNT samples can be explained in relation to the number of accessible active sites on the TiNT catalyst's surface. In particular, in samples modified with 0.8 mM Fe, iron species contribute to overall photocatalysis as active photocatalytic sites and, in total, improve photocatalytic activity of pure TiNT. The decrease of the photocatalytic activity at higher Fe-compound concentrations can be attributed to the shielding effect [57] of FeOOH and Fe_2O_3 species on the TiNTs surface that prevent the access of BT to the active sites on TiNT surface. Furthermore, if a layer of FeOOH or Fe_2O_3 completely covers the surface of TiO_2 nanotubes, photogenerated electrons and holes have to migrate over longer distances from the surface of the Fe-species to the TiO_2 [42]. Moreover, the pronounced absorption of irradiation below 400 nm by FeOOH [58] and stable absorption of irradiation throughout the UV and visible part of solar spectrum typical for Fe_2O_3 [59], might be responsible for blocking the available incident irradiation necessary for the initiation of radical reaction cycle on the TiNT surface.

The proposed mechanism responsible for an increase of the photocatalytic activity of FeOOH or Fe_2O_3 @TiNT heterostructures could be explained taking into consideration the mechanism of charge carrier (electrons and holes) transfer in coupled semiconductor systems (including TiO_2), and narrowing of the band gap in a semiconductor [60,61]. During the heterojunction formation (FeOOH or Fe_2O_3 in contact with TiO_2), electrons move from TiO_2 conduction band (CB) to Fe_2O_3 CB, while holes move from valence band (VB) of Fe_2O_3 to TiO_2 VB. As a consequence, excess holes close to TiO_2 , and excess electrons close to FeOOH or Fe_2O_3 form an internal electric field directed from TiO_2 to Fe_2O_3 . Such electric field leads to the opposite direction of charge carriers diffusion during photocatalytic process [60]. Therefore, under visible light irradiation, photogenerated electrons are injected from the conduction band (CB) of FeOOH or Fe_2O_3 to that of TiO_2 inhibiting the recombination of photogenerated charge carriers. As a result, high concentration of electrons in the CB of TiO_2 is obtained (photoexcited electrons from TiO_2 VB and electrons injected into TiO_2 from FeOOH or Fe_2O_3) and they can generate superoxide ions (Figure 9). At the same time, holes from the TiO_2 VB

will move to the VB of FeOOH or Fe₂O₃, resulting in the high concentration of holes in the VB of FeOOH or Fe₂O₃ in heterostructures [29,50,60,62–65]. Oxidative degradation of the BT involves holes from TiO₂ and hydroxyl radicals formed at the photocatalyst/liquid interface [55]. Minella et al. [66] studied the photocatalytic degradation of 1H-benzotriazole, formation of the principal intermediates, the relationship between the degradation rate and pH and the fate of the organic nitrogen under UV-irradiated TiO₂. Their work gave insights into the mechanism of photocatalytic transformation of BT, therefore we anticipate the similar chemical reaction mechanisms in our system. Under UV/Vis irradiation, unstable Fe(II) complex is formed and it can oxidize the hydroxide ion, returning to Fe(III) and forming hydroxide radical [63]. This is the most important benefit contributing solar light photocatalytic activity because iron species serve as co-catalysts on the surface of TiNT.

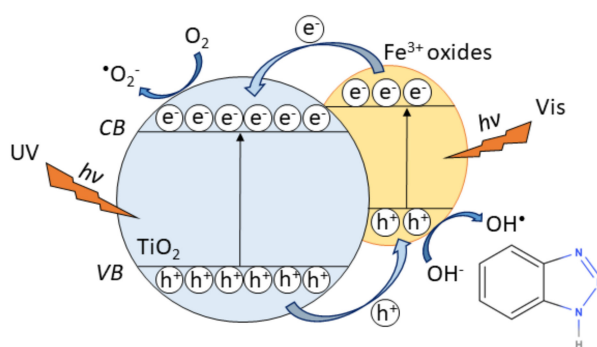


Figure 9. Schematic representation of the proposed mechanism for charge transfer pathways on FeOOH@TiNT and Fe₂O₃@TiNT for degradation of 1H-benzotriazole.

3. Materials and Methods

3.1. Synthesis of FeOOH and Fe₂O₃ Modified Photocatalysts

TiO₂ nanotube arrays were obtained by anodizing titanium metal foil (1.5 × 1.5 cm, thickness 0.25 mm, 99.7%, Sigma Aldrich, Steinheim, Germany) [48]. Before anodization, substrates were cleaned in an ultrasonic cleaner in acetone (C₃H₅OH, p.a., Fluka), ethanol (C₂H₅OH, 99.8%, Fluka) and deionized water. Afterwards, anodization was carried out in a teflon reactor with a conventional two-electrode cell using direct current (Pt foil served as a counter electrode and Ti-foil was used as the anode). As an electrolyte, ethylene glycol (C₂H₆O₂, 99.5%, Sigma-Aldrich) solution containing 0.3 wt. % ammonium fluoride (NH₄F, 99.9%, Sigma-Aldrich) and 12 vol. % deionized H₂O was used. The anodization process was carried out at 60 V for three hours at the room temperature. After anodization, Ti foil was ultrasonically cleaned in deionized water, dried using nitrogen gas and thermally treated in a tube furnace at 450 °C for two hours in air (heating rate = 2 °C/min) in order to obtain anatase nanotubes (TiNT).

Modification with FeOOH or Fe₂O₃

As-prepared TiNT were immersed in an autoclave reactor with a teflon insert containing an aqueous solution of iron (III) chloride (FeCl₃, 97%, Honeywell) in various concentrations (0.8 mM, 8 mM and 80 mM, respectively). The reactor was heated at 80 °C for three hours. This procedure gave us titanium nanotubes modified with FeOOH in various fractions depending on starting FeCl₃ concentrations. Therefore, we denoted prepared samples accordingly: 0.8 mM_FeOOH@TiNT, 8 mM_FeOOH@TiNT and 80 mM_FeOOH@TiNT. Samples were ultrasonically cleaned in deionized water and dried using nitrogen gas. In order to obtain Fe₂O₃@TiNT, as prepared FeOOH@TiNT samples were heated at 400 °C for two hours (heating rate = 1 °C/min). Above mentioned treatment gave us titanium nanotubes modified with Fe₂O₃ (0.8 mM_Fe₂O₃@TiNT, 8 mM_Fe₂O₃@TiNT and 80 mM_Fe₂O₃@TiNT).

3.2. Photocatalytic Activity

3.2.1. Photoreactor Setup

Photocatalytic activity tests were performed in flow-through reactor, i.e., small photocatalytic cell (SPC). The SPC and experimental procedure was previously described in detail by [51]. Unmodified and FeOOH or Fe₂O₃ modified photocatalysts were placed at the bottom of the photocatalytic cell ($V = 30$ mL) perpendicular to the source of irradiation. A full-spectrum compact fluorescent bulb with high UVB intensity (JBL Reptile Desert UV, 15 W, 6500 K) was used as irradiation source. Isoactinic conditions were obtained by placing the bulb in a special conical housing with a reflective inner surface. The intensities at the samples' surface were measured by UVP UVX radiometer. Intensities were $I_{UVB} = 1.35$ mW/cm² and $I_{UVA} = 2.45$ mW/cm². The working solution of 1H-benzotriazole (BT) (C₆H₅N₃, 99%, Acros Organics, NJ, USA) was prepared by mixing together 5 mg of BT and 1 L of deionized water ($C_0 = 5$ mg dm⁻³). Prior to photocatalytic experiments, working solutions were recirculated ($Q = 120$ mL/min) in the dark over the samples for 15 min in order to achieve the sorption equilibrium.

Measurements were performed in time interval from 0 to 60 min (0 min, 15 min, 30 min, 45 min and 60 min). For each irradiation time, at least three parallel samples of the aqueous solution ($V = 85$ µL) were taken from the flow cell. To study the photolysis of the BT, control experiments without photocatalyst were performed. Furthermore, all experiments were performed in triplets to discard possible experimental error and to check the stability of the photocatalysts.

3.2.2. HPLC-UV Analysis

1H-benzotriazole for standard preparation was purchased from Acros Organics, NJ, USA (C₆H₅N₃, 99%). MiliQ[®] water (18.2 MΩcm⁻¹; purified by MiliQ water purification system (Millipore, Bedford, MA, USA)) with analytical-grade formic acid (FA) (Acros Organics, Geel, Belgium) and HPLC gradient-grade methanol (J.T. Baker, Center Valley, PA, USA) were used for mobile phase preparation. Stock solution of 1H-benzotriazole was prepared as 1 mg/mL solution in MeOH. Working solutions were prepared from stock solution as 10 µg/mL and 1 µg/mL solution, respectively, by dilution with MiliQ water. The calibrants were prepared by further dilution of working solutions with MiliQ water in the range of 0.1–50 µg/mL.

HPLC-UV analysis was carried out using an Agilent Technologies 1200 series HPLC system equipped with a binary pump, a vacuum membrane degasser, an automated auto sampler and DAD detector (Agilent Technologies Inc., Palo Alto, CA, USA). The separation was performed on Synergi Fusion-RP 80 Å column (150 × 2 mm, 4 µm particle size) (Phenomenex, Torrance, CA, USA). Solvents for the analysis were 0.1% formic acid (FA) in water (solvent A) and methanol (solvent B). The gradient was applied as follows: 0 min 75% A, 0–3 min 75% A–50% A, 3–10 min 50% A–10% A, 10–15 min 10% A, 15.1–20 min 75% A. Flow rate was 0.5 mL/min. Sample injection was 5 µL. Retention time of 1H-benzotriazole was 5.1 min. The ultraviolet detector was adjusted at 258 nm for absorption measurement. The calibration curve was obtained by linear regression; the peak area obtained at 258 nm was plotted versus the analyte concentration. Least-squares linear regression gave Spearman correlation coefficients of $R^2 = 0.9991$ with the regression lines of $y = 50.14x - 5.33$. During analysis, all instrumental blank samples were negative and areas of calibration samples at 5 µg/mL were repeatable. All data acquisition and processing was performed using Agilent MassHunter software (Santa Clara, CA 95051, United States).

3.3. Raman Spectroscopy

Confocal micro-Raman spectroscopy measurements of FeOOH and Fe₂O₃ modified TiO₂ nanotubes were performed using Jobin Yvone T64000 (HORIBA Jobin Yvon GmbH, Bensheim, Germany) with solid state laser operated at 532.5 nm for excitation. The objective with 50× magnification and large working distance was used. The power of the laser at the sample was 24 mW and it was optimized to avoid heating in the focus of the laser beam that could induce phase transition of TiO₂.

3.4. Scanning Electron Microscopy (SEM) and Energy-Dispersive X-ray Spectroscopy (EDS)

The morphology and elemental composition of the photocatalysts' surface was investigated using scanning electron microscopy (SEM) on a Tescan Vega 3 Easyprobe microscope operating at 15 kV accelerating voltage and 5 mm working distance. The information about elemental composition of the samples was obtained by EDS Bruker XFlash 4010-M energy dispersive X-ray analyzer attached to the above-described microscope.

3.5. Grazing Incidence X-ray Diffraction (GIXRD) Analysis

The crystalline structure of the samples was investigated using Siemens D5000 diffractometer in parallel beam geometry with Cu K- α radiation, a point detector and a collimator in front of the detector. Grazing incidence X-ray diffraction (GIXRD) scans were performed with the constant incidence angle $\alpha_i = 1^\circ$, guaranteeing that the information contained in the scattered signal covers the entire sample's volume, i.e., ensuring a maximum diffraction yield. The diffracted spectra were collected with a curved position sensitive detector (RADICON) in the angular range of $2\theta = 20\text{--}85^\circ$.

3.6. UV-Vis Diffuse-Reflectance Spectroscopy

The optical properties of the photocatalysts were measured by UV-vis diffuse reflectance spectroscopy using Perkine-Elmer Lambda 25 spectrophotometer with an integrated sphere assembly in a wavelength range from 200 to 1100 nm. The band gap energies of unmodified and FeOOH or Fe₂O₃ modified TiNT were calculated from spectra using Kubelka-Munk equation [67].

4. Conclusions

A series of FeOOH and Fe₂O₃ modified immobilized TiO₂ catalysts were synthesized by hydrothermal synthesis method using aqueous solution of FeCl₃ as Fe-modification source in three different concentrations (0.8 mM, 8 mM and 80 mM). Results demonstrated that modifications with 0.8 mM FeOOH showed approximately two times increase in photocatalytic activity under UV/solar irradiation in comparison to as-synthesized TiO₂ nanotubes (similar photocatalytic activity as commercial P25). The increase in the photocatalytic activity for the lowest Fe concentration (0.8 mM) can be attributed to a synergistic effect between iron species and TiO₂. Coupling TiNT with FeOOH on the surface resulted in higher absorption in the visible light region, i.e., allowing photocatalysts to harness visible light which contributed to the enhanced degradation of 1H-benzotriazole. On the other hand, decrease of the photocatalytic activity at higher Fe-compounds concentrations (8 mM and 80 mM) is due to the shielding effect of FeOOH and Fe₂O₃ species on the TiO₂ surface that prevent the access of BT and available incident irradiation to the active TiO₂ sites necessary for the initiation of radical reaction cycle. Since the synthesis of immobilized FeOOH@TiNT heterostructures is simple and inexpensive, and catalysts samples showed better photocatalytic activity than commercial P25 TiO₂, proposed syntheses could be a promising way to obtain more efficient photocatalysts used in a scaled-up flow-through reactor systems for wastewater purification.

Author Contributions: Conceptualization, A.G. and V.K.; investigation, V.K., M.R., L.R., K.S., T.Č., A.G., L.B.; validation, T.Č., A.G. and I.G.; resources, A.G., I.G., L.B. and K.S.; data curation, L.R., K.S., L.B.; writing—original draft preparation, T.Č.; writing—review and editing, A.G. and I.G.; visualization, T.Č.; supervision, A.G.; funding acquisition, A.G., I.G. All authors have read and agreed to the published version of the manuscript.

Funding: This work was supported by the Ministry of science and education of Croatia under the project HrZZ-IP-2018-01-5246, Centre of Excellence for Advanced Materials and Sensing Devices, Ruđer Bošković Institute, Zagreb, Croatia KK.01.1.1.01.0001 and by European Regional Development Fund (ERDF) under the project "Waste & Sun for photocatalytic degradation of micropollutants in water" (OS-Mi), KK.01.1.1.04.0006.

Conflicts of Interest: The authors declare no conflict of interest. The funders had no role in the design of the study; in the collection, analyses, or interpretation of data; in the writing of the manuscript, or in the decision to publish the results.

References

1. Fujishima, A.; Honda, K. Electrochemical Photolysis of Water at a Semiconductor Electrode. *Nat. Cell Biol.* **1972**, *238*, 37–38. [\[CrossRef\]](#)
2. Cao, C.; Yan, J.; Zhang, Y.; Zhao, L. Stability of titania nanotube arrays in aqueous environment and the related factors. *Sci. Rep.* **2016**, *6*, 23065. [\[CrossRef\]](#) [\[PubMed\]](#)
3. Phoothong, W.; Pavasupree, S.; Mekprasart, W.; Pecharapa, W. Synthesis of low-cost titanium dioxide-based heterojunction nanocomposite from natural ilmenite and leucosene for electrochemical energy storage application. *Curr. Appl. Phys.* **2018**, *18*, S44–S54. [\[CrossRef\]](#)
4. Tao, H.; Zhou, M.; Wang, K.; Cheng, S.; Jiang, K. Glycol Derived Carbon- TiO₂ as Low Cost and High Performance Anode Material for Sodium-Ion Batteries. *Sci. Rep.* **2017**, *7*, 43895. [\[CrossRef\]](#) [\[PubMed\]](#)
5. Paz, Y. Application of TiO₂ photocatalysis for air treatment: Patents' overview. *Appl. Catal. B Environ.* **2010**, *99*, 448–460. [\[CrossRef\]](#)
6. Lee, S.-Y.; Park, S.-J. TiO₂ photocatalyst for water treatment applications. *J. Ind. Eng. Chem.* **2013**, *19*, 1761–1769. [\[CrossRef\]](#)
7. Zhang, M.; Chen, T.; Wang, Y. Insights into TiO₂ polymorphs: Highly selective synthesis, phase transition, and their polymorph-dependent properties. *RSC Adv.* **2017**, *7*, 52755–52761. [\[CrossRef\]](#)
8. Zhang, J.; Zhou, P.; Liu, J.; Yu, J. New understanding of the difference of photocatalytic activity among anatase, rutile and brookite TiO₂. *Phys. Chem. Chem. Phys.* **2014**, *16*, 20382–20386. [\[CrossRef\]](#)
9. Ge, M.; Cao, C.; Huang, J.; Li, S.; Chen, Z.; Zhang, K.-Q.; Al-Deyab, S.S.; Lai, Y. A review of one-dimensional TiO₂ nanostructured materials for environmental and energy applications. *J. Mater. Chem. A* **2016**, *4*, 6772–6801. [\[CrossRef\]](#)
10. Noman, M.T.; Ashraf, M.A.; Ali, A. Synthesis and applications of nano-TiO₂: A review. *Environ. Sci. Pollut. Res.* **2019**, *26*, 3262–3291. [\[CrossRef\]](#)
11. Gong, D.; Grimes, C.A.; Varghese, O.K.; Hu, W.; Singh, R.S.; Chen, Z.; Dickey, E.C. Titanium oxide nanotube arrays prepared by anodic oxidation. *J. Mater. Res.* **2001**, *16*, 3331–3334. [\[CrossRef\]](#)
12. Guo, Q.; Zhou, C.; Ma, Z.; Yang, X. Fundamentals of TiO₂ Photocatalysis: Concepts, Mechanisms, and Challenges. *Adv. Mater.* **2019**, *31*, e1901997. [\[CrossRef\]](#) [\[PubMed\]](#)
13. Yin, S.; Aita, Y.; Komatsu, M.; Sato, T.J. One-Step Hydrothermal Synthesis of Nitrogen-Doped Titanium Oxide Nanotubes with Enhanced Visible Light Photocatalytic Activity. *Eur. Ceram. Soc.* **2006**, *26*, 2735–2742. [\[CrossRef\]](#)
14. Zhang, W.; Luo, N.; Huang, S.; Weng, Y.-T.; Wei, M. Sulfur-Doped Anatase TiO₂ as an Anode for High-Performance Sodium-Ion Batteries. *ACS Appl. Energy Mater.* **2019**, *2*, 3791–3797. [\[CrossRef\]](#)
15. Zhang, Z.; Tang, W.; Neurock, M.; Yates, J.J.T. Electric Charge of Single Au Atoms Adsorbed on TiO₂(110) and Associated Band Bending. *J. Phys. Chem. C* **2011**, *115*, 23848–23853. [\[CrossRef\]](#)
16. Hao, Q.-Q.; Wang, Z.; Wang, T.; Ren, Z.; Zhou, C.; Yang, X. Role of Pt Loading in the Photocatalytic Chemistry of Methanol on Rutile TiO₂(110). *ACS Catal.* **2018**, *9*, 286–294. [\[CrossRef\]](#)
17. Plodinec, M.; Grčić, I.; Willinger, M.G.; Hammud, A.; Huang, X.; Panžić, I.; Gajović, A. Black TiO₂ nanotube arrays decorated with Ag nanoparticles for enhanced visible-light photocatalytic oxidation of salicylic acid. *J. Alloys Compd.* **2019**, *776*, 883–896. [\[CrossRef\]](#)
18. Sohrabi, S.; Akhlaghian, F. Surface investigation and catalytic activity of iron-modified TiO₂. *J. Nanostructure Chem.* **2015**, *6*, 93–102. [\[CrossRef\]](#)
19. Heciak, A.; Morawski, A.W.; Grzmil, B.; Mozia, S. Cu-modified TiO₂ Photocatalysts for Decomposition of Acetic Acid with Simultaneous Formation of C1–C3 Hydrocarbons and Hydrogen. *Appl. Catal.* **2013**, *140–141*, 108–114. [\[CrossRef\]](#)
20. He, Z.; Tang, J.; Shen, J.; Chen, J.; Song, S. Enhancement of photocatalytic reduction of CO₂ to CH₄ over TiO₂ nanosheets by modifying with sulfuric acid. *Appl. Surf. Sci.* **2016**, *364*, 416–427. [\[CrossRef\]](#)
21. Ruzicka, J.-Y.; Abu Bakar, F.; Thomsen, L.; Cowie, B.C.; McNicoll, C.; Kemmitt, T.; Brand, H.E.A.; Ingham, B.; Andersson, G.G.; Golovko, V.B. XPS and NEXAFS study of fluorine modified TiO₂ nano-ovals reveals dependence of Ti3+ surface population on the modifying agent. *RSC Adv.* **2014**, *4*, 20649–20658. [\[CrossRef\]](#)
22. Radoičić, M.; Šaponjić, Z.V.; A Janković, I.; Ćirić-Marjanović, G.; Ahrenkiel, S.P.; Čomor, M.I. Improvements to the photocatalytic efficiency of polyaniline modified TiO₂ nanoparticles. *Appl. Catal. B Environ.* **2013**, *136–137*, 133–139. [\[CrossRef\]](#)

23. Chen, J.; Wang, N.; Ma, H.; Zhu, J.; Feng, J.; Chen, J. Facile Modification of a Polythiophene/TiO₂ Composite Using Surfactants in an Aqueous Medium for an Enhanced Pb(II) Adsorption and Mechanism Investigation. *J. Chem. Eng. Data* **2017**, *62*, 2208–2221. [\[CrossRef\]](#)
24. De Filpo, G.; Pantuso, E.; Armentano, K.; Formoso, P.; Di Profio, G.; Poerio, T.; Fontananova, E.; Meringolo, C.; Mashin, A.I.; Nicoletta, F.P. Chemical Vapor Deposition of Photocatalyst Nanoparticles on PVDF Membranes for Advanced Oxidation Processes. *Membranes* **2018**, *8*, 35. [\[CrossRef\]](#) [\[PubMed\]](#)
25. Huang, B.; Yang, W.; Wen, Y.; Shan, B.; Chen, R. Co₃O₄-Modified TiO₂ Nanotube Arrays via Atomic Layer Deposition for Improved Visible-Light Photoelectrochemical Performance. *ACS Appl. Mater. Interfaces* **2014**, *7*, 422–431. [\[CrossRef\]](#) [\[PubMed\]](#)
26. Lu, Y.; Chen, T.; Chen, X.; Qiu, M.; Fan, Y. Fabrication of TiO₂-doped ZrO₂ nanofiltration membranes by using a modified colloidal sol-gel process and its application in simulative radioactive effluent. *J. Membr. Sci.* **2016**, *514*, 476–486. [\[CrossRef\]](#)
27. Sun, Y.; Gao, Y.; Zeng, J.; Guo, J.; Wang, H. Enhancing visible-light photocatalytic activity of Ag-TiO₂ nanowire composites by one-step hydrothermal process. *Mater. Lett.* **2020**, *279*, 128506. [\[CrossRef\]](#)
28. Tian, Z.; Yu, N.; Cheng, Y.; Wang, Z.; Chen, Z.; Zhang, L. Hydrothermal Synthesis of Graphene/TiO₂/CdS Nanocomposites as Efficient Visible-light-driven Photocatalysts. *Mater. Lett.* **2017**, *194*, 172–175. [\[CrossRef\]](#)
29. Rao, G.; Zhao, H.; Chen, J.; Deng, W.; Jung, B.; Abdel-Wahab, A.; Batchelor, B.; Li, Y. FeOOH and Fe₂O₃ co-grafted TiO₂ photocatalysts for bisphenol A degradation in water. *Catal. Commun.* **2017**, *97*, 125–129. [\[CrossRef\]](#)
30. Ozkan, S.; Cha, G.; Mazare, A.; Schmuki, P. TiO₂ nanotubes with different spacing, Fe₂O₃ decoration and their evaluation for Li-ion battery application. *Nanotechnology* **2018**, *29*, 195402. [\[CrossRef\]](#)
31. Van Viet, P.; Huy, T.H.; You, S.-J.; Van Hieu, L.; Thi, C.M. Hydrothermal synthesis, characterization, and photocatalytic activity of silicon doped TiO₂ nanotubes. *Superlattices Microstruct.* **2018**, *123*, 447–455. [\[CrossRef\]](#)
32. Theerthagiri, J.; Chandrasekaran, S.; Salla, S.; Elakkiya, V.; Senthil, R.; Nithyadharseni, P.; Maiyalagan, T.; Micheal, K.; Ayeshamariam, A.; Arasu, M.V.; et al. Recent developments of metal oxide based heterostructures for photocatalytic applications towards environmental remediation. *J. Solid State Chem.* **2018**, *267*, 35–52. [\[CrossRef\]](#)
33. Spanu, D.; Recchia, S.; Mohajernia, S.; Schmuki, P.; Altomare, M. Site-selective Pt dewetting on WO₃-coated TiO₂ nanotube arrays: An electron transfer cascade-based H₂ evolution photocatalyst. *Appl. Catal. B Environ.* **2018**, *237*, 198–205. [\[CrossRef\]](#)
34. Wei, L.; Yu, C.; Zhang, Q.; Liu, H.; Wang, Y. TiO₂-based heterojunction photocatalysts for photocatalytic reduction of CO₂ to solar fuels. *J. Mater. Chem. A* **2018**, *6*, 22411–22436. [\[CrossRef\]](#)
35. Spanu, D.; Santo, V.D.; Malara, F.; Naldoni, A.; Turolla, A.; Antonelli, M.; Dossi, C.; Marelli, M.; Altomare, M.; Schmuki, P.; et al. Photoelectrocatalytic oxidation of As (III) over hematite photoanodes: A sensible indicator of the presence of highly reactive surface sites. *Electrochim. Acta* **2018**, *292*, 828–837. [\[CrossRef\]](#)
36. Singh, P.; Sharma, K.; Hasija, V.; Sharma, V.; Sharma, S.; Raizada, P.; Singh, M.; Saini, A.K.; Hosseini-Bandegharai, A.; Thakur, V.K. Systematic review on applicability of magnetic iron oxides-integrated photocatalysts for degradation of organic pollutants in water. *Mater. Today Chem.* **2019**, *14*, 100186. [\[CrossRef\]](#)
37. Sakamoto, Y.; Noda, Y.; Ohno, K.; Koike, K.; Fujii, K.; Suzuki, T.M.; Morikawa, T.; Nakamura, S. First principles calculations of surface dependent electronic structures: A study on β-FeOOH and γ-FeOOH. *Phys. Chem. Chem. Phys.* **2019**, *21*, 18486–18494. [\[CrossRef\]](#)
38. Jelle, A.A.; Hmadeh, M.; O'Brien, P.G.; Perovic, D.D.; Ozin, G.A. Photocatalytic Properties of All Four Polymorphs of Nanostructured Iron Oxyhydroxides. *ChemNanoMat* **2016**, *2*, 1047–1054. [\[CrossRef\]](#)
39. Mishra, M.; Chun, D.-M. α-Fe₂O₃ as a photocatalytic material: A review. *Appl. Catal. A Gen.* **2015**, *498*, 126–141. [\[CrossRef\]](#)
40. Liu, C.; Tong, R.; Xu, Z.; Kuang, Q.; Jiang, Y.; Zheng, L. Efficiently enhancing the photocatalytic activity of faceted TiO₂ nanocrystals by selectively loading α-Fe₂O₃ and Pt co-catalysts. *RSC Adv.* **2016**, *6*, 29794–29801. [\[CrossRef\]](#)
41. Nasirian, M.; Bustillo-Lecompte, C.F.; Mehrvar, M. Photocatalytic Efficiency of Fe₂O₃/TiO₂ for the Degradation of Typical Dyes in Textile Industries: Effects of Calcination Temperature and UV—Assisted Thermal Synthesis. *J. Environ. Manag.* **2017**, *196*, 487–498. [\[CrossRef\]](#) [\[PubMed\]](#)

42. Zhang, M.; Xu, Z.; Liang, J.; Zhou, L.; Zhang, C. Potential Application of Novel TiO₂/β-FeOOH Composites for Photocatalytic Reduction of Cr (VI) with an Analysis of Statistical Approach. *Int. J. Environ. Sci. Technol.* **2014**, *12*, 1669–1676. [\[CrossRef\]](#)
43. Kuang, S.; Yang, L.; Luo, S.; Cai, Q. Fabrication, characterization and photoelectrochemical properties of Fe₂O₃ modified TiO₂ nanotube arrays. *Appl. Surf. Sci.* **2009**, *255*, 7385–7388. [\[CrossRef\]](#)
44. Cong, Y.; Li, Z.; Zhang, Y.; Wang, Q.; Xu, Q. Synthesis of α-Fe₂O₃/TiO₂ nanotube arrays for photoelectro-Fenton degradation of phenol. *Chem. Eng. J.* **2012**, *191*, 356–363. [\[CrossRef\]](#)
45. Giger, W.; Schaffner, C.; Kohler, H.-P.E. Benzotriazole and Tolyltriazole as Aquatic Contaminants. 1. Input and Occurrence in Rivers and Lakes†. *Environ. Sci. Technol.* **2006**, *40*, 7186–7192. [\[CrossRef\]](#) [\[PubMed\]](#)
46. Ohsada, T.; Izumi, F.; Fujiki, Y. Raman spectrum of anatase, TiO₂. *J. Raman Spectrosc.* **1978**, *7*, 321–324. [\[CrossRef\]](#)
47. Hanesch, M. Raman spectroscopy of iron oxides and (oxy)hydroxides at low laser power and possible applications in environmental magnetic studies. *Geophys. J. Int.* **2009**, *177*, 941–948. [\[CrossRef\]](#)
48. Mandić, V.; Plodinec, M.; Kereković, I.; Jurać, K.; Janicki, V.; Gracin, D.; Gajović, A.; Moguš-Milanković, A.; Willinger, M. Tailoring anatase nanotubes for the photovoltaic device by the anodization process on behalf of microstructural features of titanium thin film. *Sol. Energy Mater. Sol. Cells* **2017**, *168*, 136–145. [\[CrossRef\]](#)
49. Li, J.; Xu, J.; Dai, W.-L.; Li, H.; Fan, K. Direct hydro-alcohol thermal synthesis of special core-shell structured Fe-doped titania microspheres with extended visible light response and enhanced photoactivity. *Appl. Catal. B Environ.* **2009**, *85*, 162–170. [\[CrossRef\]](#)
50. Han, H.; Riboni, F.; Karlicky, F.; Kment, S.; Goswami, A.; Sudhagar, P.; Yoo, J.; Lei, W.; Tomanec, O.; Petr, M.; et al. α-Fe₂O₃/TiO₂ 3D hierarchical nanostructures for enhanced photoelectrochemical water splitting. *Nanoscale* **2017**, *9*, 134–142. [\[CrossRef\]](#)
51. Čižmar, T.; Panžić, I.; Salamon, K.; Grčić, I.; Radetić, L.; Marčec, J.; Gajović, A. Low-Cost Synthesis of Cu-Modified Immobilized Nanoporous TiO₂ for Photocatalytic Degradation of 1H-Benzotriazole. *Catalysts* **2019**, *10*, 19. [\[CrossRef\]](#)
52. Garg, S.; Yadav, M.; Chandra, A.; Sapra, S.; Gahlawat, S.; Ingole, P.P.; Pap, Z.; Hernádi, K. Biofabricated BiOI with enhanced photocatalytic activity under visible light irradiation. *RSC Adv.* **2018**, *8*, 29022–29030. [\[CrossRef\]](#)
53. Song, X.; Boily, J.-F. Surface and Bulk Thermal Dehydroxylation of FeOOH Polymorphs. *J. Phys. Chem. A* **2016**, *120*, 6249–6257. [\[CrossRef\]](#) [\[PubMed\]](#)
54. Shi, Z.-Q.; Liu, Y.-S.; Xiong, Q.; Cai, W.-W.; Ying, G.-G. Occurrence, toxicity and transformation of six typical benzotriazoles in the environment: A review. *Sci. Total. Environ.* **2019**, *661*, 407–421. [\[CrossRef\]](#)
55. Lee, J.-E.; Kim, M.-K.; Lee, J.-Y.; Lee, Y.-M.; Zoh, K.-D. Degradation kinetics and pathway of 1H-benzotriazole during UV/chlorination process. *Chem. Eng. J.* **2019**, *359*, 1502–1508. [\[CrossRef\]](#)
56. Mawhinney, D.B.; Vanderford, B.J.; Snyder, S.A. Transformation of 1H-Benzotriazole by Ozone in Aqueous Solution. *Environ. Sci. Technol.* **2012**, *46*, 7102–7111. [\[CrossRef\]](#)
57. Slamet; Nasution, H.W.; Purnama, E.; Kosela, S.; Gunlazuardi, J. Photocatalytic reduction of CO₂ on copper-doped Titania catalysts prepared by improved-impregnation method. *Catal. Commun.* **2005**, *6*, 313–319. [\[CrossRef\]](#)
58. Guijarro, N.; Bornoz, P.; Prévot, M.; Yu, X.; Zhu, X.; Johnson, M.; Jeanbourquin, X.; Le Formal, F.; Sivula, K. Evaluating spinel ferrites MFe₂O₄ (M = Cu, Mg, Zn) as photoanodes for solar water oxidation: Prospects and limitations. *Sustain. Energy Fuels* **2018**, *2*, 103–117. [\[CrossRef\]](#)
59. Li, X.; Wang, Z.; Zhang, Z.; Chen, L.; Cheng, J.; Ni, W.; Wang, B.; Xie, E. Light Illuminated α-Fe₂O₃/Pt Nanoparticles as Water Activation Agent for Photoelectrochemical Water Splitting. *Sci. Rep.* **2015**, *5*, 9130. [\[CrossRef\]](#)
60. Mei, Q.; Zhang, F.; Wang, N.; Yang, Y.; Wu, R.; Wang, W. TiO₂/Fe₂O₃ heterostructures with enhanced photocatalytic reduction of Cr (VI) under visible light irradiation. *RSC Adv.* **2019**, *9*, 22764–22771. [\[CrossRef\]](#)
61. Anandan, S.; Ikuma, Y.; Niwa, K. An Overview of Semi-Conductor Photocatalysis: Modification of TiO₂ Nanomaterials. *Solid State Phenom.* **2010**, *162*, 239–260. [\[CrossRef\]](#)
62. Peng, L.; Xie, T.; Lu, Y.; Fan, H.; Wang, D. Synthesis, photoelectric properties and photocatalytic activity of the Fe₂O₃/TiO₂ heterogeneous photocatalysts. *Phys. Chem. Chem. Phys.* **2010**, *12*, 8033–8041. [\[CrossRef\]](#) [\[PubMed\]](#)

63. Zhu, T.; Ong, W.L.; Zhu, L.; Ho, G.W. TiO₂ Fibers Supported β -FeOOH Nanostructures as Efficient Visible Light Photocatalyst and Room Temperature Sensor. *Sci. Rep.* **2015**, *5*, 10601. [[CrossRef](#)] [[PubMed](#)]
64. Kment, S.; Riboni, F.; Pausova, S.; Wang, L.; Wang, L.; Han, H.; Hubicka, Z.; Krysa, J.; Schmuki, P.; Zboril, R. Photoanodes based on TiO₂ and α -Fe₂O₃ for solar water splitting—superior role of 1D nanoarchitectures and of combined heterostructures. *Chem. Soc. Rev.* **2017**, *46*, 3716–3769. [[CrossRef](#)] [[PubMed](#)]
65. Mohamed, H.H.; Alomair, N.A.; Akhtar, S.; Youssef, T.E. Eco-Friendly synthesized α -Fe₂O₃/TiO₂ Heterojunction with Enhanced Visible Light Photocatalytic Activity. *J. Photochem.* **2019**, *382*, 111951. [[CrossRef](#)]
66. Minella, M.; De Laurentiis, E.; Pellegrino, F.; Prozzi, M.; Bello, F.D.; Maurino, V.; Minero, C. Photocatalytic Transformations of 1H-Benzotriazole and Benzotriazole Derivates. *Nanomaterials* **2020**, *10*, 1835. [[CrossRef](#)]
67. López, R.; Gómez, R. Band-gap energy estimation from diffuse reflectance measurements on sol–gel and commercial TiO₂: A comparative study. *J. Sol-Gel Sci. Technol.* **2012**, *61*, 1–7. [[CrossRef](#)]

Publisher’s Note: MDPI stays neutral with regard to jurisdictional claims in published maps and institutional affiliations.



© 2020 by the authors. Licensee MDPI, Basel, Switzerland. This article is an open access article distributed under the terms and conditions of the Creative Commons Attribution (CC BY) license (<http://creativecommons.org/licenses/by/4.0/>).